Frontiers in Heat and Mass Transfer

Tech Science Press

https://doi.org/10.32604/fhmt.2026.086281

ARTICLE

Performance Study of Cu Nanofluids in Spectral Beam Splitting Photovoltaic/Thermal Systems

Guofen Rui[1], Xiangyu Hu[2], Jingyu Cao[3,4,*], Yibo Zhang[2], Yangyang Zhu[2] and Haifei Chen[1,2,*]

[1]Changzhou University Huaide College, Changzhou University, Taizhou, China
[2]School of Energy, Changzhou University, Changzhou, China
[3]College of Civil Engineering, Hunan University, Changsha, China
[4]Key Laboratory of Building Safety and Energy Efficiency of Ministry of Education, Hunan University, Changsha, China

*Corresponding Authors: Jingyu Cao. Email: jycao@hnu.edu.cn; Haifei Chen. Email: chfs@cczu.edu.cn

Received: 27 May 2026; Accepted: 17 July 2026; Published: 31 August 2026

ABSTRACT: Spectral beam splitting is a promising approach for thermally decoupling photovoltaic and photothermal processes in PV/T systems. However, existing liquid spectral splitters still suffer from insufficient short-wavelength absorption and/or the high cost of noble-metal nanoparticles. In this study, a water-based Cu@SiO_2 nanofluid was developed as a low-cost absorption/transmission spectral splitting filter for monocrystalline silicon PV/T systems. The full solar spectrum considered in this system covers both photovoltaic and thermal utilization, while 750–1000 nm was selected only as the target transmission window for the c-Si cell. This window was chosen because c-Si cells can effectively utilize this near-infrared band, whereas the short-wavelength radiation can be absorbed by Cu@SiO_2 nanoparticles for heat generation and the longer-wavelength infrared radiation can be mainly absorbed by the water-based fluid for thermal recovery. FDTD simulations, combined with Mie scattering theory and the Beer–Lambert law, were used to evaluate the optical response of Cu nanoparticles and optimize the particle size. Cu@SiO_2 nanoparticles were synthesized using an ammonia-free coating method to suppress Cu oxidation and core corrosion, and the prepared nanofluids were tested outdoors under real solar irradiation. The results show that Cu nanoparticles with a diameter of 50 nm provide a favorable balance between absorption and scattering. At mass concentrations of 0.02, 0.035, and 0.05 wt%, the overall system efficiencies were 56.84%, 60.12%, and 63.38%, respectively. The highest electrical efficiency was 9.30% at 0.02 wt%, whereas the highest thermal efficiency was 48.25% at 0.05 wt%. These results indicate that Cu@SiO_2 nanofluids can improve the energy utilization of the tested SBS-PV/T system, although the nanofluid concentration should be optimized to balance thermal gain and photovoltaic transmittance loss.

KEYWORDS: Solar energy; nanofluid; full spectrum; photovoltaic/thermal

1 Introduction

In today's world, the consumption of fossil fuels is substantial. Due to their environmental unfriendliness, the use of fossil fuels has led to a series of environmental issues [1]. Driven by the demand for sustainable development, there has been a significant push for the further research and application of new energy sources, particularly solar energy. Among these, the most widely utilized are solar thermal and photovoltaic applications [2]. In photovoltaic applications, the solar spectrum ranges from 200 to 2500 nm, which is a continuous distribution. However, current photovoltaic cells are limited by the band-gap of the materials used [3]. The spectral range that can be absorbed and converted into electrical energy by photovoltaic cells

differs from the full spectrum of sunlight [4]. Fig. 1 [5] presents a comparison of the response spectra of various photovoltaic cells with the solar spectral irradiance.

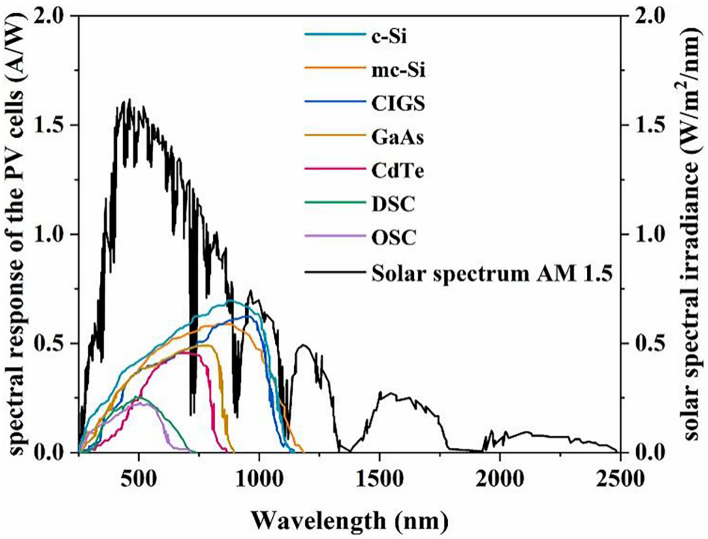

Figure 1: Solar spectrum distribution and spectral response curves of different photovoltaic cells [5].

Although modern crystalline silicon solar cells can respond to a broad spectral range of approximately 300/350–1100 nm [6], their spectral response is wavelength-dependent. Recent studies have shown that the short-wavelength response of Si photovoltaic modules can be improved by luminescent down-shifting and advanced anti-reflection/passivation strategies. Therefore, in this study, 750–1000 nm is not regarded as the full response range of c-Si cells, but is selected as the target high-transmittance window for the present $Cu@SiO_2$ nanofluid spectral splitter. The remaining spectral regions are assigned mainly to photothermal recovery, so that the incident solar spectrum can be utilized by both the PV and PT components of the SBS-PV/T system [5,7]. This difference between absorption and response can lead to thermal issues in photovoltaic cells during use, and the electrical efficiency is negatively correlated with the operating temperature [8]. Therefore, to address this issue, photovoltaic (PV) and photothermal (PT) systems are integrated for combined utilization, Das et al. [9] study investigated the use of heat transfer pipes arranged on the backside of the panel, which improved the thermal load of the photovoltaic system. The system achieved a maximum thermal efficiency of 63.6% and an electrical efficiency of 11.73%, which is 1.68% higher than that of a standalone PV system. Rubaiee et al. [10] conducted a simulation analysis of various fluids used as heat transfer media and found that when the mass flow rate of GO/EG:W: graphene oxide dispersed in an ethylene glycol/water mixture, is 0.07 kg/s and the mass concentration is 0.01%, the electrical efficiency and thermal efficiency of the PV/T system are 13.5% and 76%, respectively. Compared to single photovoltaic or photothermal systems, this integrated approach can utilize all the solar radiation incident on the cell surface and maintain the electrical efficiency of the photovoltaic cells. However, this utilization structure cannot avoid the thermal coupling issue between the PV and PT systems.

Therefore, in recent years, many scholars have investigated spectral beam splitting technologies to thermally decouple conventional PV/T systems. Existing spectral splitting PV/T systems can be generally classified into several configurations, such as trough or concentrating systems, mirror-based systems, solid optical filters, and liquid absorption/transmission filters. Widyolar et al. [11] applied spectral splitting to a trough concentrating PV/T system and improved the overall system efficiency. Huang et al. [12] further analyzed the efficiency limits of concentrating spectral-splitting hybrid PV/T collectors and emphasized

the importance of optical filtering and energy matching. In addition to concentrating systems, mirror-based spectral management has also been proposed. Yu et al. [13] introduced the PVMirror concept, in which selective reflection and transmission are used for hybrid solar conversion. Solid or interference-type filters have also been widely studied because of their compact structure and clear spectral selectivity. Mojiri et al. [14] developed a hybrid receiver combining direct absorption with wave-interference light filtering, while Liew and Lee [15] numerically compared hybrid PV/T systems using different spectral bandpass filters. However, solid filters and mirror-based systems usually involve fixed splitting windows, additional optical components, or higher structural complexity.

Based on the above, researchers have conducted more in-depth and extensive studies on liquid spectral splitting. Meraje et al. [16] used ZnO nanoparticles to prepare nanofluids with different mass fractions based on a water:EG (50:50) solution. Simulations were used to obtain the irradiance distribution after spectral splitting, and the electrical and thermal efficiencies of the system were calculated. The findings indicate that ZnO nanofluids can effectively split the spectrum and enhance the performance of CPV/T systems. The highest efficiency achieved was 85.7%, with an electrical efficiency of 3.73% and a thermal efficiency of 76.1%. This represents a 19.63% improvement compared to systems without spectral splitting, and the highest temperature of the splitter was 350.68 K. Liang et al. [17] also focused on ZnO spectral splitting nanofluids as their research subject. They used the overall effective spectral transmittance coefficient as the evaluation metric for the spectral transmittance of the nanofluid. The overall effective spectral transmittance of the water-ZnO nanofluid was 21.54% higher than that of cells containing water-polyaniline and water-Cu_9S_5 nanofluids. Similarly, as a metal oxide, Fe_3O_4 was studied by Abd El-Samie et al. [18], through three-dimensional numerical simulations, they explored various base fluids and comprehensively considered the effects of concentration, flow rate, and radiation intensity on the hybrid system. They found that as the concentration increases, the system's overall efficiency slightly rises, primarily due to the increase in thermal efficiency, while the electrical efficiency decreases sharply, from the energetic viewpoint, the deionized water-based Fe_3O_4 nanofluid performed best. Jiang et al. [19] prepared four different mass fractions of ITO-EG nanofluids, the best one of them, its average transmittance and absorbance are 69.1% and 30.9%, when applied to a novel PV/T system, they achieved an electrical efficiency of 17.7% and a thermal efficiency of 18.5%.

However, in the aforementioned nanofluids, the transmittance across the entire short-wavelength range is relatively high. To design a filter that more closely resembles an ideal filter, i.e., to enhance absorption in the 300 to 750 nm wavelength range, researchers have begun exploring the use of metal nanoparticles with localized surface plasmon resonance (LSPR) effects as spectral splitting nanofluids. The LSPR effect allows metal nanoparticles to strongly absorb light within their resonant wavelength range and convert it into heat [20]. Metal nanoparticles with LSPR effects include Au, Ag, Cu, Al, etc. Among these, Au and Ag have received extensive attention and have yielded significant results in recent research. Hassani et al. [21] studied the application of Ag/H_2O nanofluids in PV/T systems, further demonstrating that spectral splitting PV/T systems are a promising method of energy utilization. The article argued that from the perspective of ExPBT (Exergy PayBack Time), the payback period for spectral splitting PV/T systems is 2 years, which is the shortest, followed by PV/T systems and standalone PV systems at 2.55 years and 3.48 years, respectively.

Subsequently, more researchers have been exploring the use of Ag nanofluids in the field of spectral splitting. Xia et al. [22] explored the spectral splitting performance of Ag, CNT, and Ag/CNT nanofluids at different concentrations. The filtering efficiency of the CNT/Ag nanofluid solar spectral splitting filter reached its peak at a concentration of 5×10^6 μg/m^3, with a filtering efficiency of 18.3%. This represents a 37.1% increase in filtering efficiency compared to previous levels. Compared to Ag and CNT nanofluids, the thermal efficiency and electrical efficiency of the CNT/Ag nanofluid PV/T system were improved by 9.9% and

7.2%, respectively, and by 15% and 1.4%, respectively. Wang et al. [23] explored the application of Ag/$COSO_4$-PG nanofluids in scenarios close to the ideal spectral splitting window. Through simulation calculations, the photovoltaic efficiency of the photovoltaic module can reach 30.2%, with a photovoltaic efficiency of 11.9%. The thermal efficiency can reach 49.3%, and it is positively correlated with the inlet flow rate of the nanofluid and negatively correlated with the initial temperature. Subsequently, Wang built an experimental setup and further explored the synergistic effect of Ag and $COSO_4$ and its engineering applications. The results showed that compared to Ag-based water nanofluids, the system's thermal efficiency and exergy efficiency were further improved with Ag/$COSO_4$ nanofluids [24].

More recently, nanofluid- and film-based spectral beam splitting technologies have been further developed for hybrid PV/T systems. Jiao et al. reviewed nanofluid-based SBS-PV/T systems and identified spectral matching, dispersion stability and cost as key challenges [5]. Recent studies have explored SiO_2/water, CNT/Ag, ZnO-SiO_2 and Al@Ag nanofluids to tune PV-band transmission and non-PV-band absorption [22,25–27]. In parallel, solid filters such as SiNx/Cu and Nb_2O_5/SiO_2 multilayer films have been designed to provide well-defined spectral windows [28,29]. However, noble-metal cost, limited short-wavelength absorption, colloidal stability, fixed splitting windows and thin-film fabrication complexity remain concerns. Therefore, developing a low-cost and oxidation-resistant Cu-based nanofluid with suitable short-wavelength absorption and PV-band transmission is still meaningful for SBS-PV/T systems.

Although a variety of nanoparticles have been researched and utilized for spectral beam splitting (SBS), for monocrystalline silicon photovoltaic cells with an ideal spectral splitting window of 750 to 1000 nm, the aforementioned nanoparticles, whether non-metallic or those with surface plasmon resonance effects such as Au and Ag, exhibit a significant deficiency in absorption in the short-wavelength range. Table 1 presents the spectral transmittance of the aforementioned spectral splitters. Furthermore, a significant factor limiting the development of Au and Ag nanoparticles with surface plasmon resonance effects in spectral beam splitting (SBS) is their high cost, aside from their ability to absorb the ultraviolet portion of the spectrum [30].

Table 1: Compact comparison of recent nanofluid- and film-based spectral beam splitters.

Ref.	Spectral Splitter	Type	Key Performance	Main Limitation
Yang et al. [25]	SiO_2/water	Nanofluid	Optimal 0.10 wt.%; max efficiency 51.93%.	Limited LSPR absorption.
Xia et al. [22]	CNT/Ag	Nanofluid	PV transmittance and non-PV absorbance improved.	Ag cost; broadband CNT absorption.
Zhang et al. [26]	ZnO-SiO_2/water	Nanofluid	Improved filtering and PV/T merit function.	Oxide-based selectivity.
Wang et al. [27]	Al@Ag/water	Nanofluid	Short-wave transmittance reduced by up to 13%.	Ag shell adds cost.
Zhang et al. [28]	SiNx/Cu film	Film	T = 72.9%; R = 89.7%.	Sputtering complexity.
Said et al. [29]	Nb_2O_5/SiO_2 film	Film	580–1100 nm wideband transmission.	Complex multilayer design.

This study investigates the use of Cu nanoparticles, which exhibit surface plasmon resonance effects, as spectral splitters. This approach aims to address the issues of insufficient absorption in the short-wavelength range and high costs associated with Au and Ag nanoparticles. Deionized water, which exhibits strong absorption in the 1100 to 2500 nm range, is chosen as the base fluid, focusing on the 300 to 1000 nm wavelength range. The transmittance model of the nanofluid is constructed using Mie scattering theory and the Beer-Lambert law. By exploring the effects of particle size and concentration on the performance of the spectral splitter, optimal parameters for the splitter are obtained. Cu nanofluids are prepared to validate the simulation results, and transmittance comparisons are conducted. These fluids are then applied in PV/T systems. Additionally, the authors address the issue of Cu nanoparticles being prone to oxidation. Following the step-by-step coating method proposed by Li et al. [31], protective treatment was applied to Cu nanoparticles, resulting in the preparation of $Cu@SiO_2$ nanoparticles and nanofluids. The practical application of Cu nanofluids was explored.

As summarized in Table 2, representative nanofluid spectral beam splitters are compared in terms of nanoparticle type, base fluid, study method, transmittance window, key findings, and differences from the present work. This comparison is intended to clarify the material selection and research gap addressed in this study: unlike previous ZnO-, ITO-, CNT/Ag-, Ag-, or Au-based nanofluids, the novelty of this work lies in the integration of Cu-based LSPR absorption, optical parameter optimization, and outdoor PV/T performance validation. The SiO_2 shell is used as a protective strategy to improve the practical stability of Cu nanoparticles in aqueous nanofluids.

Table 2: Comparison of representative nanofluid spectral beam splitters with the present study.

Nanoparticle	Ref.	Base Fluid	Study Type	Transmittance Window	Key Findings	Difference from the Present Work
ZnO	[16]	Water/EG (50:50)	Sim. + Exp.	300–1000 nm	Samples A-F filtered 19.58–80.75% of incident spectrum; peak temperature was 350.68 K; MF increased from 1.076 to 1.184.	Used non-metallic ZnO rather than LSPR-active $Cu@SiO_2$ nanoparticles.
ZnO/Cu_9S_5	[17]	Water	Sim. + Exp.	400–1200 nm	Water-ZnO increased the overall effective spectral-transmittance coefficient by 8.74% relative to water-Cu_9S_5.	Focused on oxide/sulfide nanofluids, not Cu-based core-shell splitters.
ITO	[19]	EG	Sim. + Exp.	250–1250 nm	Electrical and thermal efficiencies were 17.7% and 18.5%, respectively.	Used ITO-EG nanofluid with lower reported thermal performance.

(Continued)

Table 2 (continued)

Nanoparticle	Ref.	Base Fluid	Study Type	Transmittance Window	Key Findings	Difference from the Present Work
CNT	[22]	Water	Sim. + Exp.	300–1100 nm	Thermal/electrical efficiencies increased by 9.9%/7.2% relative to CNT and by 15.0%/1.4% relative to Ag.	Broadband CNT absorption lacks Cu plasmonic spectral selectivity.
Ag			Sim. + Exp.	600–1100 nm		Used costly Ag instead of lower-cost protected Cu nanoparticles.
CNT/Ag			Sim. + Exp.	700–1100 nm		Relied on CNT/Ag hybrid rather than Cu@SiO_2 nanofluid.
Ag	[23]	$CoSO_4$-PG	Sim.	750–1100 nm	Optical efficiency reached 95.5%; electrical and thermal efficiencies reached 11.9% and 49.3%.	Mainly simulation-based and used Ag/$CoSO_4$-PG fluid.
Ag	[24]	Water	Exp.	500–1400 nm	Thermal, electrical, and overall exergy efficiencies were 56.0%, 8.5%, and 19.6%, respectively.	Used Ag-based fluids rather than oxidation-resistant Cu@SiO_2.
		$CoSO_4$ solution		500–1200 nm		
Ag and Au	[32]	Water	Exp.	750–1000 nm	Thermal efficiency increased by 6.8% with Au nanoparticles and 4.8% with Ag nanoparticles.	Used noble metals, whereas this work uses lower-cost Cu@SiO_2.

2 Method

The Finite-Difference Time-Domain (FDTD) method, initially proposed by Yee, is now widely used in the spectral splitting of nanofluids. It is a powerful tool for exploring the optical properties of nanoparticles [33]. FDTD Solutions enables researchers to investigate a range of variables and modifications in natural and synthetic systems. In this paper, it is primarily used to simulate and analyze the absorption and scattering characteristics of different Cu nanoparticles, detecting their absorption and scattering cross-sections.

2.1 Modeling

In this study, Cu nanoparticles of different sizes were simulated using the software. The FDTD simulation region was set to 1 μm, with perfect matching layer boundary conditions. The simulation region and grid were automatically generated by the software, with finer grid processing inside to ensure simulation accuracy. A total field scattered field source (TFST) was selected, and monitors were placed within the simulation region to monitor absorption and scattering performance. The wavelength range of the light

source was set from 300 to 1000 nm. The refractive index of the materials was obtained from the software's built-in material library.

The PML boundaries were used to absorb outgoing electromagnetic waves and minimize artificial reflection from the computational boundaries, thereby approximating an optically open environment. The Cu nanoparticle was assumed to be spherical and surrounded by deionized water, which is consistent with the nanofluid environment considered in the subsequent transmittance model. A non-uniform mesh generated by the software was adopted, and local mesh refinement was applied near the nanoparticle surface and the metal–fluid interface, where strong field gradients are expected due to localized surface plasmon resonance. This mesh treatment was used to improve the numerical accuracy of the near-field and cross-section calculations. The wavelength-dependent optical constants of Cu were taken from the built-in material database of the FDTD software. The absorption and scattering cross-sections of the nanoparticles can be obtained based on FDTD Solutions. Subsequently, the scattering cross-section, absorption cross-section, and extinction cross-section of the particles can be calculated using classical Mie scattering theory [33].

Since the simulated particles are spherical and the surrounding medium is homogeneous, classical Mie scattering theory provides the theoretical basis for interpreting the absorption, scattering, and extinction behavior. Therefore, the FDTD results were analyzed together with the Mie-theory framework to confirm the physical consistency of the size-dependent optical response. The present FDTD calculation was mainly used to compare the relative optical behavior of Cu nanoparticles with different diameters, while the final spectral-splitting performance was further examined using experimental transmittance spectra.

2.2 NP Optical Performance Analysis

To further investigate the absorption performance of nanoparticles in the 300 to 750 nm photothermal band and the transmission performance in the 750 to 1000 nm photovoltaic band, the absorption and scattering powers of different particle sizes in the above two spectral bands were calculated based on the AM1.5 standard solar spectrum.

Particle size, as a key factor influencing the optical properties of nanoparticles, including absorption cross-section (Absorption cross-section, Abs), scattering cross-section (Scattering cross-section, Sca), and extinction cross-section (Extinction cross-section, Ext), is one of the main focuses of this study. Additionally, to quantify the suitability of particle size, which mainly involves the absorption performance in the 300 to 750 nm photothermal band and the transmission performance in the 750 to 1000 nm photovoltaic band, the total extinction power (Total extinction efficiency, $P_{Ext,total}$), relative efficiency (Relatively efficient, η_{Rel}) and extinction efficiency, η_{Ext}, were introduced to comprehensively evaluate the impact of particle size.

$$P_{Ext,total} = \int_{330}^{1000} Ext(\lambda) \cdot I_{AM1.5}(\lambda) d(\lambda) \tag{1}$$

$$\eta_{Rel} = \frac{P_{Ext,total} - P_{Ext,pv}}{P_{Ext,total}} \times 100\% \tag{2}$$

$$\eta_{Ext} = \frac{Ext(\lambda)}{S} \tag{3}$$

where $Ext(\lambda)$ is the Extinction cross section at the corresponding wavelength of λ, it can be calculated as:

$$Ext(\lambda) = Abs(\lambda) + Sca(\lambda) \tag{4}$$

and $Abs(\lambda)$ is Absorption cross section at the corresponding wavelength of λ, $Sca(\lambda)$ is Scattering cross section at the corresponding wavelength of λ. Both of them can be obtained from FDTD Solutions. S is the

cross-sectional area of the nanoparticle in the direction of the incident light, in this paper, it refers to the cross-sectional area of the spherical nanoparticle passing through its center. And $I_{AM1.5}(\lambda)$ is the standard solar radiation intensity at the corresponding wavelength of λ, λ is the solar radiation wavelength is the solar radiation wavelength, range from 300 to 1000 nm, $P_{Ext,pv}$ is the extinction power in the Photovoltaic band. $P_{Ext,pv}$ can be calculated as [34]:

$$P_{Ext,pv} = \int_{750}^{1000} Ext(\lambda) \cdot I_{AM1.5}(\lambda) d(\lambda) \tag{5}$$

2.3 Nanofluid Transmission Modeling

Typically, the transmittance of nanofluids is calculated using the Lambert-Beer law, which is given by the following formula:

$$\tau_{NF} = EXP(-\sigma_{NF} \cdot L) \tag{6}$$

In the formula, σ_{NF} is the extinction coefficient of the nanofluid, L is the optical path length., σ_{NF} It consists of two parts: the extinction coefficient of the nanoparticle ensemble (σ_{NPs}) and the extinction coefficient of the base fluid (σ_{BF}) [35], that is

$$\sigma_{NF} = \sigma_{NPs} + \sigma_{BF} \tag{7}$$

Since the concentration of the nanofluid in this paper is low, much less than 0.6% [36,37], the interaction forces between nanoparticles can be neglected, so σ_{NPs} can be calculated using the following formula [34]:

$$\sigma_{NPs} = \frac{3 f_v \eta_{Ext}}{2d} \tag{8}$$

This assumption corresponds to the dilute-suspension approximation. Under this condition, the inter-particle electromagnetic coupling and multiple scattering effects are weak, and the extinction of the nanofluid can be approximated by the sum of independent-particle extinction and base-fluid absorption. Therefore, the single-particle optical response obtained from FDTD can be linked to the macroscopic transmittance of the nanofluid through the Beer–Lambert law.

In the formula, f_v is the mass concentrations of the nanoparticles, and d is the diameter of the nanoparticles.

$$\sigma_{BF} = \frac{4\pi\kappa}{\lambda} \tag{9}$$

In the formula, κ is the extinction coefficient of the base fluid, and the data comes from Handbook of Optical Constants of Solids.

The optical simulation of Cu nanoparticles was conducted to determine the optimal Cu core size for spectral beam splitting, since the plasmonic absorption and scattering characteristics are mainly governed by the Cu core. However, bare Cu nanoparticles are chemically unstable and susceptible to oxidation and corrosion during conventional coating processes. Therefore, after the Cu core size was optimized by FDTD simulation, an ammonia-free stepwise coating method was employed to synthesize Cu@SiO_2 core–shell nanoparticles. In this way, the Cu core provides the required spectral absorption behavior, while the SiO_2 shell improves chemical stability and dispersion stability. The prepared Cu@SiO_2 nanofluids were then characterized by spectral transmittance measurements and further tested in the SBS-PV/T system under real sunlight conditions.

3 Preparation of NPs and Nanofluid

3.1 Ammonia-Free Synthesis of Cu@SiO_2

The conventional Stöber method employs ammonia as an alkaline source, which can lead to etching of the nanoparticle cores [31]. This issue is particularly problematic when Cu is used as the core, as it results in the degradation of Cu nanoparticles. Consequently, the traditional Stöber method is unsuitable for preparing Cu@SiO_2 nanoparticles. To address this limitation, an ammonia-free step-by-step coating process, as proposed by Li et al. [31], was adopted for the synthesis of Cu@ SiO_2.

The detailed preparation procedure was as follows:

Cu nanoparticles (1 g; purity 99%; diameter 50 nm; MERYER Co., Ltd., China) were dispersed in 50 mL of ethanol (95%; Yonghua Chemical Co., Ltd., China), and the pH was adjusted to 9.5 using NaOH solution (purity 98%; MERYER Co., Ltd., China). Under vigorous stirring, 10 mL of TEOS solution (CP grade; Sinopharm Chemical Reagent Co., Ltd., China) was added, and additional TEOS was added every 0.5 h. After the first 1 h of addition, a small amount of NaOH solution was introduced simultaneously with each TEOS addition. The total amount of TEOS was 12 mL. After TEOS addition was completed, the mixture was stirred overnight, and the product was collected by centrifugation.

3.2 Morphological and Elemental Characterization of Cu@SiO_2 Nanoparticles

The morphology and elemental distributions of the prepared Cu@SiO_2 nanoparticles were characterized using Sigma 360, ZEISS field-emission scanning electron microscope. As shown in Fig. 2, the particles predominantly exhibit a quasi-spherical morphology. Nanoscale primary particles and larger secondary aggregates are observed, while individual particles with relatively complete spherical contours can be distinguished in the high-magnification images.

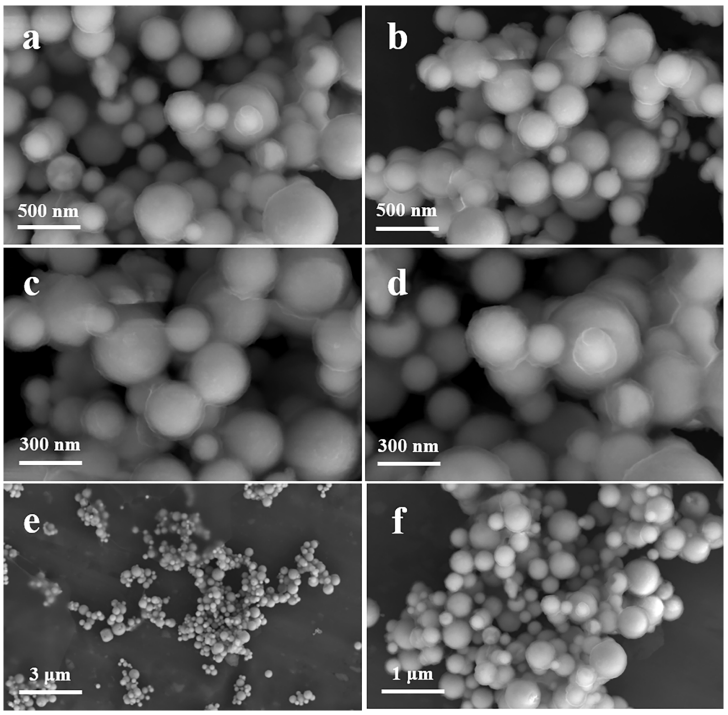

Figure 2: SEM images of the prepared Cu@SiO_2 nanoparticles at different magnifications: (**a**,**b**) Scale bars of 500 nm; (**c**,**d**) Scale bars of 300 nm; (**e**) Scale bar of 3 μm; (**f**) Scale bar of 1 μm.

Fig. 3 presents the EDS elemental maps of Cu, Si, and O. The Cu signal is distributed throughout the particle-rich regions, whereas the Si and O signals exhibit similar distributions over the Cu-containing particles. The coexistence and spatial coincidence of Cu, Si, and O confirm the presence of the silica phase and the successful deposition of SiO_2 on the Cu particles. The SEM and EDS results demonstrate that the prepared particles possess the expected morphology and elemental composition of Cu@SiO_2 nanoparticles, supporting their application in the water-based spectral-splitting nanofluid.

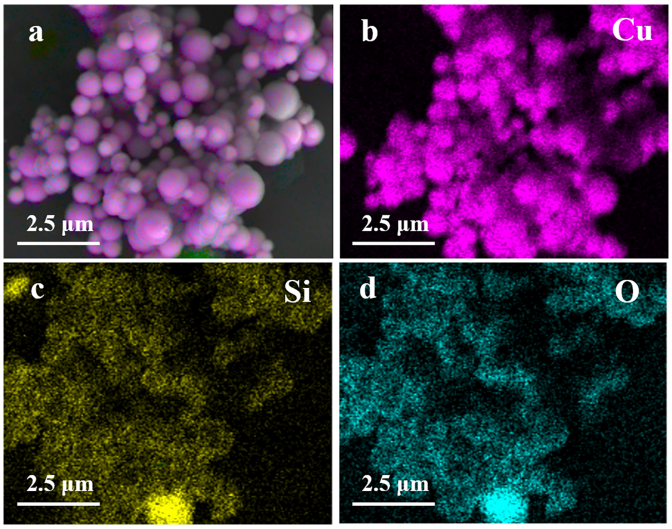

Figure 3: SEM-EDS elemental mapping of the prepared Cu@SiO_2 nanoparticles: (**a**) SEM image of the selected region and the corresponding elemental maps of (**b**) Cu, (**c**) Si, and (**d**) O.

3.3 Preparation of Cu@SiO_2 Nanofluid

In this paper, deionized water (DI) was chosen due to its strong absorption of sunlight in the infrared range, as well as its low cost and stability. The nanofluid was prepared using a two-step method. The specific steps are shown in Fig. 4: First, add the nanoparticles to DI. Stir the mixture for 2 h using a magnetic stirrer, then perform a cycle of stirring for 5 min and ultrasonic oscillation for 3 min, repeating this cycle several times until the nanofluid is uniform and stable.

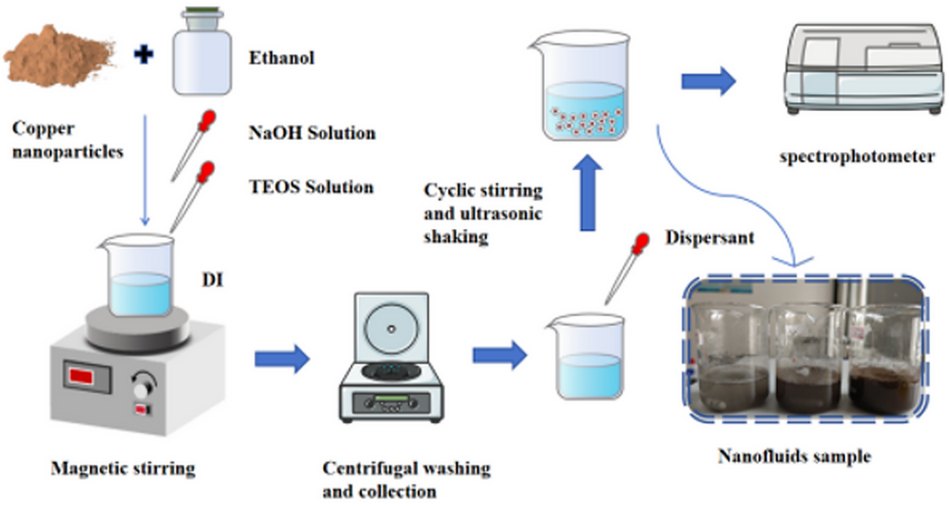

Figure 4: Nanofluid preparation schematic.

Moreover, the spectral splitter container is fabricated from cut and sealed acrylic sheets, measuring 35 by 400 mm, which corresponds to the dimensions of the photovoltaic panels employed.

It should be noted that the stability of Cu-based nanofluids is an important factor for their practical application in spectral splitting PV/T systems, because bare Cu nanoparticles are susceptible to oxidation, aggregation, and sedimentation in aqueous environments. In the present work, Cu nanoparticles were encapsulated with a SiO_2 shell using an ammonia-free stepwise coating method rather than being directly dispersed in water. The SiO_2 shell provides a protective barrier between the Cu core and the surrounding water/oxygen environment, thereby helping to suppress the oxidation of Cu nanoparticles and preserve their localized surface plasmon resonance characteristics. This core–shell structure is beneficial for maintaining the optical absorption and transmission behavior required for spectral beam splitting.

In addition to the protective coating, magnetic stirring and intermittent ultrasonication were employed during nanofluid preparation to enhance dispersion uniformity and reduce initial agglomeration [36,37]. Previous studies have demonstrated that the stability of nanofluids is closely related to surface charge, sedimentation behavior, and time-dependent optical response. Zeta potential is commonly used to evaluate the electrostatic repulsion between nanoparticles, sedimentation observation directly reflects the macroscopic dispersion state, and UV–Vis spectra can monitor the variation of optical absorption/transmission characteristics over time [38,39]. These reported stability criteria support the importance of the SiO_2 coating and dispersion treatment adopted in this work. Therefore, the prepared Cu@SiO_2 nanofluid combines the plasmonic absorption ability of Cu nanoparticles with the oxidation-resistance and dispersion-improving effect of the SiO_2 shell, making it suitable for use as an absorption/transmission spectral splitting medium in SBS-PV/T systems.

4 Experimental Setup

An experimental setup was designed and constructed to test the performance of the designed spectral splitting PV/T system under real sunlight conditions. The present system adopts a direct absorption liquid spectral splitting configuration rather than a reflective, interference-film, concentrating, or secondary-reflection design. In this configuration, the Cu@SiO_2 nanofluid layer is placed in front of the monocrystalline silicon PV module. The incident solar radiation first passes through the nanofluid spectral splitter. The 300–750 nm short-wavelength band is preferentially absorbed by Cu@SiO_2 nanoparticles for photothermal conversion, the 750–1000 nm band is transmitted to the c-Si PV cell for electricity generation, and the longer-wavelength infrared radiation is mainly absorbed by the water-based fluid for thermal recovery. Therefore, the nanofluid acts simultaneously as a spectral filter and a heat-collection medium. Fig. 5 shows the current experimental apparatus. To more closely simulate real operating conditions, the photovoltaic panel and spectral splitting device were installed at an angle, which is the optimal tilt angle for photovoltaic installation in the local area. Table 3 lists the components of the device and their specifications. Solar irradiance, ambient temperature, photovoltaic panel output voltage, output current, and electrical efficiency are all measured using a portable solar testing device. The temperatures of the photovoltaic panel and the spectral splitting fluid are measured by thermocouples and are collected and transmitted to a computer via a data acquisition system.

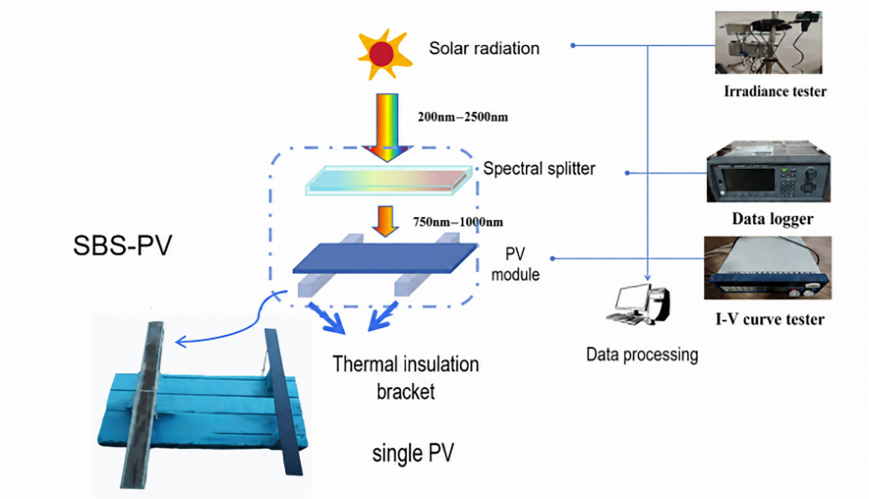

Figure 5: Schematic diagram of the experimental setup.

Table 3: Measurement instruments and precision specifications.

Equipment	Manufacturer	Model	Accuracy	Range
I–V curve tester	Jinzhou Sunshine Meteorological Technology Co., Ltd.	m9712	±0.05% ±0.015%	0–500 V 0–30 A
Solar pyranometer		TBQ-2	<5%	0–2000 W/m^2
Temperature tester		PTWD-2A	±0.1°C	−40°C–80°C
PH tester	Shanghai Yidian Scientific Instruments Co., Ltd.	PHS-3C	0.01	0.00–14.00
Data logger	Keysight Technologies	DAQ970A	±0.75%	0°C–800°C

The outdoor experiments were conducted in Changzhou, Jiangsu Province, China, under natural solar irradiation. The ambient temperature and initial device temperature are 307.93 K, with a wind speed of 1 m s^{-1}. The Cu@SiO_2 nanofluid was maintained in a quiescent state inside the sealed acrylic spectral splitter. Heat transfer within the fluid occurred through volumetric solar absorption, heat conduction, and natural convection. Each case was tested for 600 s. The initial transient thermal efficiency was calculated using the first 360 s, whereas the full 600-s data were used to characterize the temperature evolution. During the selected analysis periods, the measured solar irradiances were 924.6 ± 3.2, 916.5 ± 5.8, and 938.3 ± 2.9 W m^{-2} for the 0.02, 0.035, and 0.05 wt% cases, respectively. Repeated I–V scans were obtained during each test, with 7, 6, and 11 valid scans retained for statistical analysis. The corresponding coefficients of variation of the electrical-efficiency measurements were 0.85%, 0.72%, and 0.43%, respectively.

The photovoltaic and photothermal conversion efficiencies are calculated using the following formulas [40]:

$$\eta_{pv} = \frac{I_m V_m}{G A_{pv}} \tag{10}$$

where I_m and V_m are the current and voltage at maximum power, G is the total solar irradiance, and A_{pv} is the area of the photovoltaic panel.

$$\eta_{th} = \frac{(c_{bf}m_{bf} + c_{np}m_{np})(T_2 - T_1)}{IA_{SBS}\Delta t} \tag{11}$$

where c_{bf} and m_{bf} are the specific heat capacity and mass of the base fluid, c_{np}, m_{np} andT_2 are the specific heat capacity and mass of the nanoparticles, T_1 is the initial temperature of the spectral splitting fluid, Δt is the temperature rise time. This calculation is more accurate when the temperature of the spectral splitting fluid is low and the heat loss to the environment is minimal [41], so the first 360 s of the experiment are taken. It should be noted that the thermal efficiency calculated using Eq. (11) is defined as the initial transient thermal efficiency in this study, rather than the steady-state collector efficiency. The first 360 s was selected because the temperature difference between the nanofluid and the ambient environment was relatively small during this period, and therefore the convective and radiative heat losses were comparatively lower. Nevertheless, the heat loss was not assumed to be zero. Thus, the calculated thermal efficiency is mainly used to compare the relative short-term photothermal conversion capability of different nanofluids under identical transient conditions.

Because electrical and thermal energy differ in thermodynamic quality, an energy-equivalent efficiency rather than a thermodynamic total efficiency was used as a first-law comparative indicator of the SBS-PV/T system. The energy-equivalent efficiency and merit function are calculated as follows [42,43]:

$$\eta_{eq} = \eta_{th} + \frac{\eta_{el}}{\eta_{ref}}, \eta_{ref} = 0.38 \tag{12}$$

$$MF = \frac{w\eta_{pv,sbs} + \eta_{th}}{w\eta_{pv,unsbs}} \tag{13}$$

where $\eta_{pv,sbs}$ is the electrical efficiency of the photovoltaic cell after spectral splitting, $\eta_{pv,unsbs}$ is the electrical efficiency of the bare cell under the same conditions without spectral splitting, w is the ratio of thermal to electrical conversion, which is taken as 3 in this paper [42]. The higher the MF value, the better the performance of the system. From an exergy perspective, the electrical output has an exergy factor close to unity, whereas the recovered thermal energy should be weighted by a temperature-dependent Carnot factor.

Due to the accuracy of the experimental equipment, there must be errors in the experimental results. Assuming that z is a function of the independent variables y_1, y_2, …, y_n, z, it can be calculated by Formula (13) [44]:

$$\partial_z = \sum_{i=0}^{n}\left(\frac{df}{dy_i}\right)^2 \partial_{y_i}^2 \tag{14}$$

The results of the uncertainty analysis are shown in Table 4. According to the calculations, the experimental uncertainty for each result during the experiment did not exceed 3.5%, which indicates that the experimental results are reliable.

Table 4: Uncertainty analysis results.

Parameter	Sources of Uncertainty	Relative Uncertainty (%)
Temperature measurement (°C)	Thermocouple accuracy; ambient fluctuations	0.5–1.2
Voltage measurement (V)	Instrument accuracy; circuit fluctuations	0.3–0.8
Current measurement (A)	Instrument accuracy; circuit fluctuations	0.4–0.9
Total radiative heat transfer rate (W)	Temperature measurement error; uncertainty associated with assumptions in the radiation model	1.5–2.5
Total heat input (W)	Combined uncertainty	2.5–3.5

5 Result and Discussion

5.1 Scattering and Absorption Spectrum Analysis

Figs. 6 and 7 show the variations in the absorption cross-sectional area and scattering cross-sectional area of nanoparticles with different diameters (10, 20, 50, 80, 100 nm) in water as a function of wavelength. Within the wavelength range of 300 to 700 nm, nanoparticles with diameters greater than 50 nm exhibit strong absorption capabilities, which increase with the size of the nanoparticles. This enhancement is attributed to the stronger localized surface plasmon resonance effects associated with larger particle sizes [45].

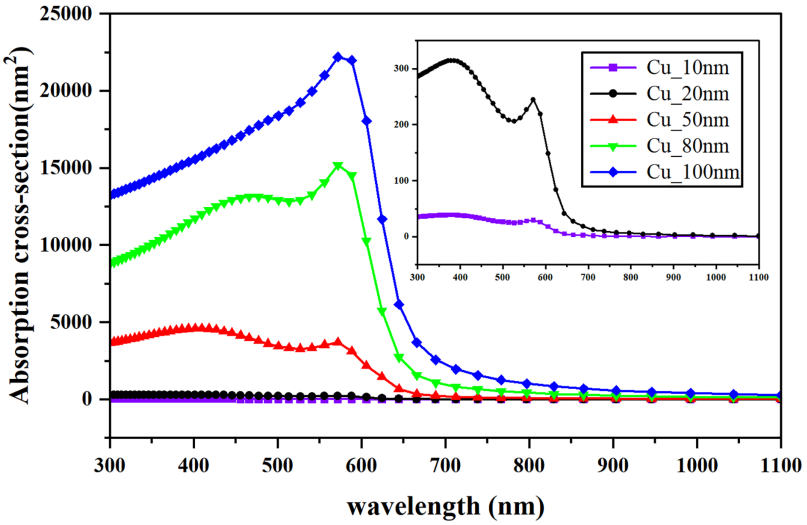

Figure 6: Absorption cross-section spectra of Cu nanoparticles with different particle sizes.

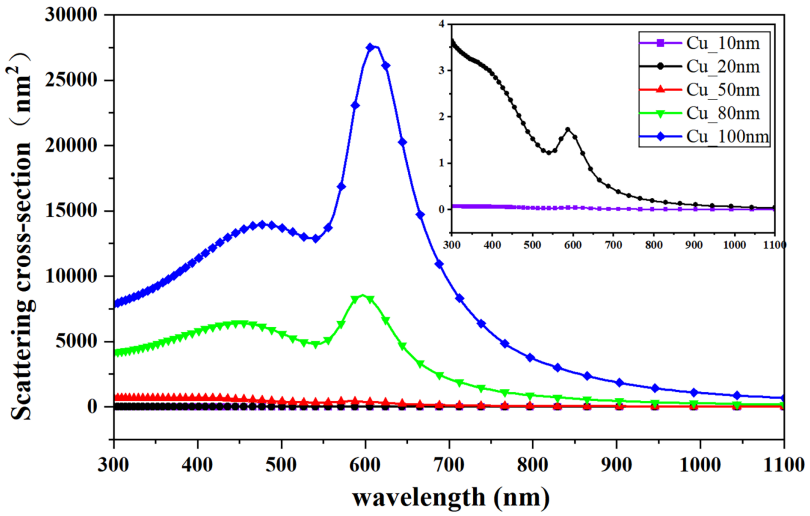

Figure 7: Scattering cross-section spectra of Cu nanoparticles with different particle sizes.

For solar radiation within this wavelength range, nanoparticles exhibit strong absorption and scattering effects. The peak absorption cross-section shifts to longer wavelengths (redshift) and increases dramatically with increasing particle size. Within the 300 to 750 nm range, the average absorption cross-sectional areas for nanoparticles with diameters of 10, 20, 50, 80, and 100 nm are 33.46, 232.23, 3373.55, 9668.44, and 14224.02 nm^2, respectively. Smaller nanoparticles show weak light absorption, indicating a weaker photothermal conversion capability. The scattering cross-section peak shows a similar trend to the absorption cross-section peak, but more pronouncedly, especially for smaller particles (10 and 20 nm) which exhibit almost no scattering effect. The results indicate that for the selection of spectral splitting fluids, Cu nanoparticles with larger diameters (50 to 100 nm) should be chosen to achieve a certain photothermal conversion capability and obtain higher photothermal conversion efficiency.

Fig. 8 illustrates the extinction cross-section spectra of Cu nanoparticles with different diameters in water. The extinction cross-section represents the combined contribution of absorption and scattering, and therefore reflects the overall light attenuation capability of the nanoparticles. As the particle diameter increases from 10 to 100 nm, the extinction intensity increases significantly, especially in the 300–750 nm spectral region. Two main extinction peaks can be observed: one located in the short-wavelength range of approximately 350–500 nm and the other in the range of approximately 550–650 nm. With increasing particle size, the second extinction peak becomes more pronounced, indicating enhanced localized surface plasmon resonance and scattering effects. This strong extinction in the 300–750 nm band is beneficial for photothermal conversion, while excessive extinction in the 750–1000 nm photovoltaic transmission window may reduce the light available to the PV cell. Therefore, the extinction spectra in Fig. 8 provide an important basis for selecting an appropriate Cu nanoparticle size for the spectral splitting nanofluid.

To this end, this study numerically analyzes this enhancement through the electric field intensity map induced by LSPR [46]. Based on the content of Fig. 9, presents the electric-field intensity distributions around Cu nanoparticles with diameters ranging from 10 to 100 nm. The electromagnetic field is mainly enhanced near the nanoparticle surface, indicating the excitation of localized surface plasmon resonance. As the particle diameter increases, the enhanced-field region becomes more spatially extended, accompanied by a stronger contribution from scattering. The 50 nm particle exhibits pronounced near-field enhancement

while avoiding the excessive scattering observed for larger particles, supporting its selection as a compromise between photothermal absorption and photovoltaic-band transmission.

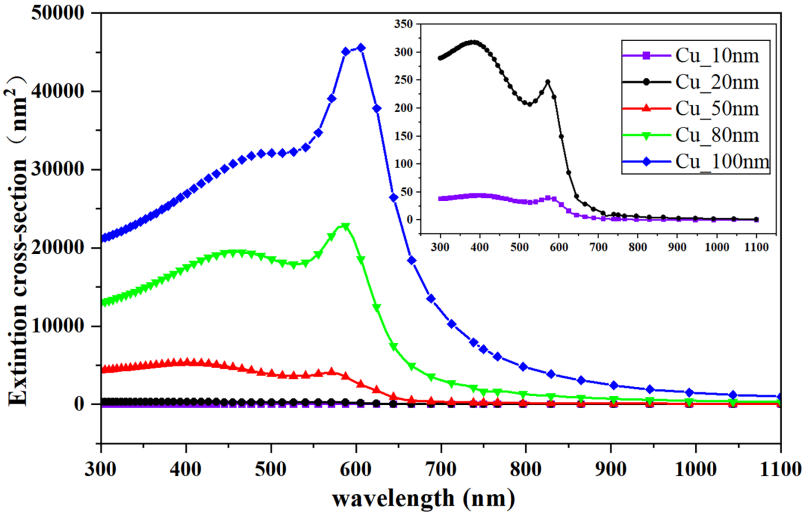

Figure 8: Extinction cross-section spectra of Cu nanoparticles with different particle sizes.

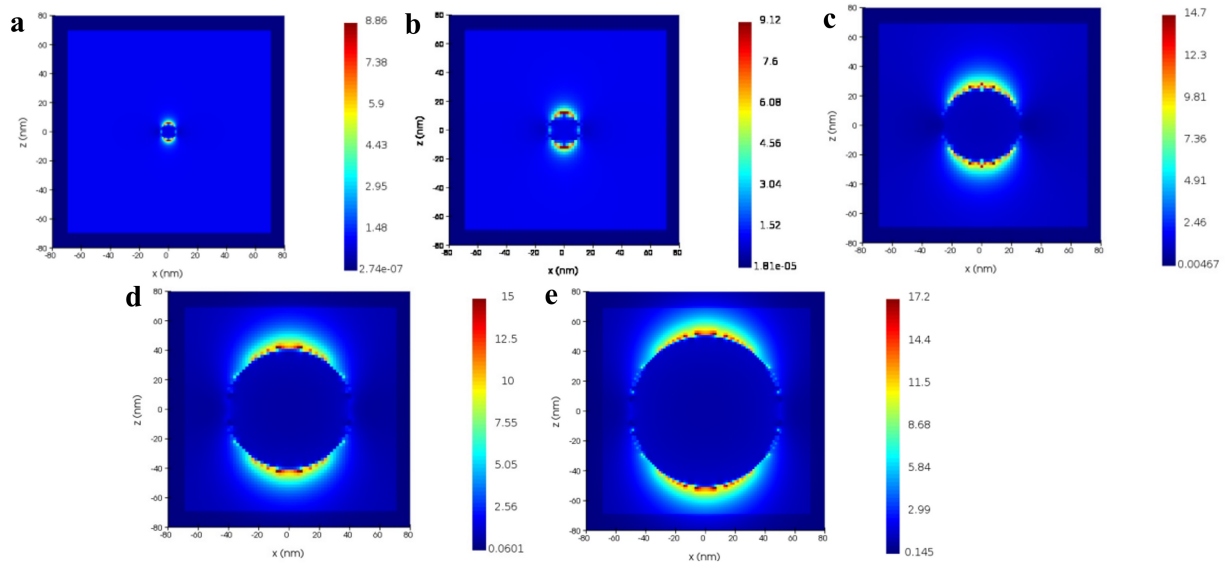

Figure 9: Electric field intensity maps of different diameters (**a**) 10 nm; (**b**) 20 nm; (**c**) 50 nm; (**d**) 80 nm; (**e**) 100 nm.

Table 5 shows that as the particle size increases, the absorption and extinction powers increase due to the enhanced surface plasmon resonance effect, but the relative efficiency decreases. To rationalize the particle-size selection, Cu nanoparticles with diameters of 10, 20, 50, 80, and 100 nm were compared in terms of absorption cross-section, scattering cross-section, extinction power, and relative spectral-splitting efficiency. Although larger particles exhibit higher absorption and extinction, excessive particle growth also enhances scattering and reduces spectral selectivity, which may attenuate the photons transmitted to the PV cell in the 750–1000 nm band. By contrast, smaller particles show insufficient absolute absorption in the photothermal band. The 50 nm particles provide a suitable compromise: they show significantly enhanced

absorption compared with 10 and 20 nm particles, while maintaining a high relative efficiency of 98.35%, higher than those of 80 and 100 nm particles. Therefore, 50 nm was selected as the optimal particle size for the present Cu-based nanofluid spectral splitter.

Table 5: Presents the relative efficiency and extinction efficiency data for nanoparticles of different diameters.

Diameter (nm)	10	20	50	80	100
$P_{Abs}(\mathrm{pW} * 10^{-9})$	$1.42 * 10^5$	$9.29 * 10^5$	$1.60 * 10^7$	$7.41 * 10^7$	$1.45 * 10^8$
$P_{Sca}(\mathrm{pW} * 10^{-9})$	196.60	952.71	$2.68 * 10^5$	$2.5 * 10^6$	$8.97 * 10^6$
$P_{Ext}(\mathrm{pW} * 10^{-9})$	$1.44 * 10^5$	$9.39 * 10^5$	$1.63 * 10^7$	$7.66 * 10^7$	$1.54 * 10^8$
η_{Rel}	98.63%	98.73%	98.35%	96.70%	94.10%

Relative efficiency is defined as $\eta_{\mathrm{Rel}} = \left(P_{\mathrm{Ext,total}} - P_{\mathrm{Ext,pv}}\right)/P_{\mathrm{Ext,total}} \times 100$, where $P_{\mathrm{Ext,pv}}$ is the solar-spectrum-weighted extinction power in the 750–1000 nm photovoltaic transmission window. Thus, a higher η_{Rel} indicates lower extinction loss in the PV band and better spectral selectivity.

Taking into account multiple particle properties such as absorption power, scattering power, extinction power, and relative efficiency, Cu nanoparticles with a diameter of 50 nm provide a good balance among these parameters. They maintain high efficiency while also having high absorption and extinction powers, which may make them an optimal choice for various applications.

5.2 Nanofluid Transmission Analysis

The spectral transmittance of Cu nanofluids and the synthesized Cu@SiO_2 was measured using a spectrophotometer, as shown in Fig. 10. These measured spectra were used to validate the spectral-splitting tendency predicted by the optical model. The model predicts that Cu-based nanofluids should strongly attenuate the 300–750 nm photothermal band while retaining relatively higher transmittance in the 750–1000 nm photovoltaic band. As shown in Fig. 10, the experimental spectra exhibit the same tendency, indicating that the modelling approach can reasonably describe the optical filtering behavior of the nanofluids. All four nanofluids can absorb most of the energy within the 300–750 nm wavelength range. However, due to different mass concentrations, nanofluids with higher concentrations have lower overall transmittance, absorbing more solar radiation energy. Nanofluids with lower mass concentrations have higher transmittance and exhibit higher transmittance within the 750–1000 nm range, which is closer to the ideal window. All nanofluid transmittance curves show a strong similarity to DI in the 950–1000 nm range, as the nanoparticles have a low extinction power in this range, and the overall transmittance is dominated by the properties of DI. Additionally, at the same concentration of Cu nanoparticles, the transmittance in the photothermal band is reduced after coating with SiO_2. This may be due to the enhanced plasmon resonance effect of Cu after coating [44], which increases the absorption capacity of the nanoparticles, the SiO_2 shell also has a certain absorption capacity for sunlight. In the photothermal band, the average spectral transmittance of the nanofluids, in order of increasing particle size, is 0.52%, 3.00%, 9.40%, and 2.87%. Coating results in a 69.44% decrease in transmittance in the photothermal band for Cu@SiO_2 nanofluids compared to Cu nanofluids.

In the photovoltaic band, the overall transmittance curves are similar, but it is noted that within the 900–950 nm range, the SiO_2 coating significantly absorbs light in the nanofluid. The average spectral transmittance of the nanofluids is 15.03%, 33.67%, 50.42%, and 45.80%. Coating results in a 9.16% decrease in transmittance in the photovoltaic band for Cu@SiO_2 nanofluids compared to Cu nanofluids. This is due to a secondary absorption peak of SiO_2 in this range, which has a significant impact. Therefore, nanofluids with lower mass concentrations may be the preferred choice as spectral splitting fluids.

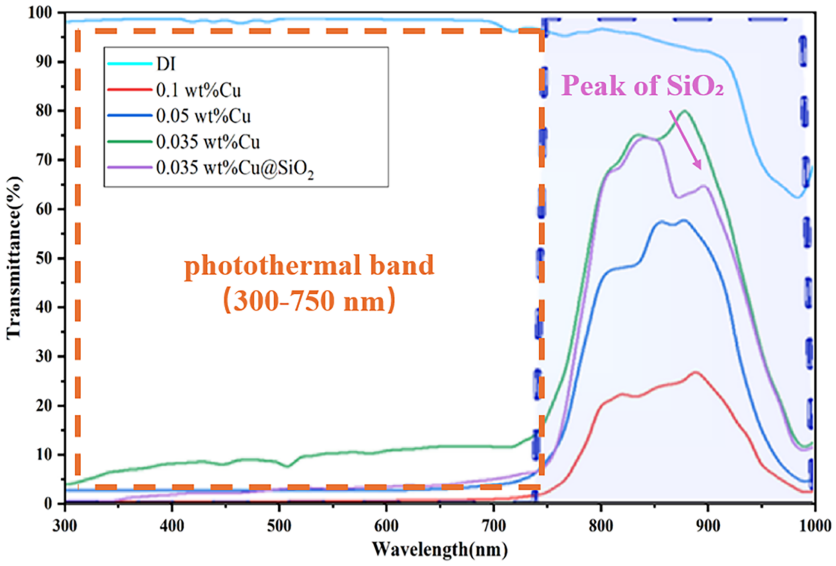

Figure 10: Spectral transmittance of Cu and Cu@SiO_2 nanofluids at different mass concentrations.

5.3 Thermal and Electrical Performance Analysis

To further evaluate the actual spectral splitting performance of Cu@SiO_2 nanofluids, this paper conducted experiments under real sunlight and performed corresponding thermal and electrical performance analyses. The merit function was used to comprehensively evaluate the overall efficiency of the system. Fig. 11a shows the temperature rise of the photovoltaic cells and the thermal of the SBS system during the first 6 min, along with the recorded solar irradiance. The test location was Changzhou, Jiangsu Province, with an ambient temperature of 308.35 K.

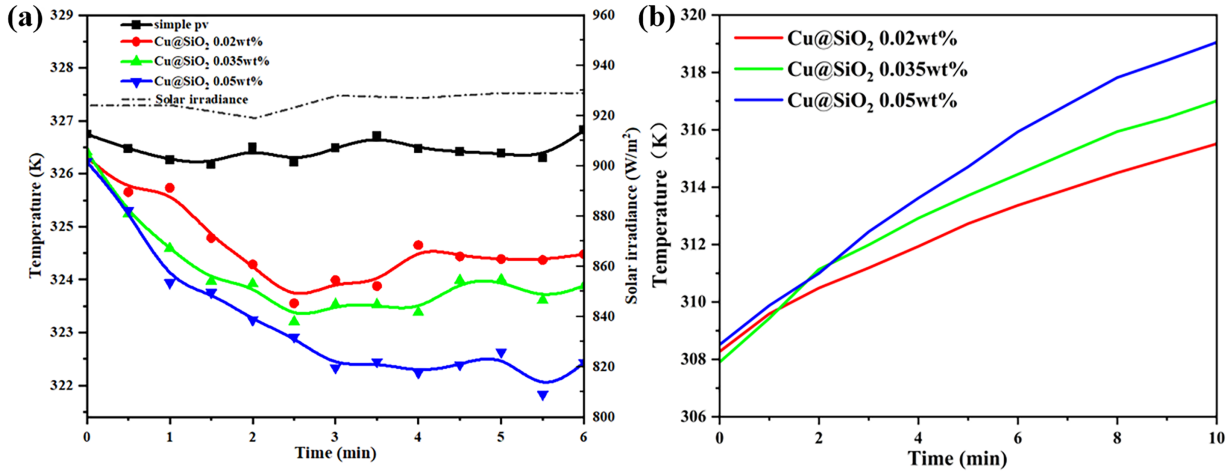

Figure 11: (**a**) Temperature change of the panel; (**b**) Temperature change of the nanofluid.

Fig. 11a shows the temperature variation of the photovoltaic panel during the first 6 min of the experiment. Under comparable solar irradiance, the temperature of the photovoltaic panel with spectral splitting is lower than that of the panel without spectral splitting, and the cooling effect becomes more pronounced as the nanofluid concentration increases. The maximum temperature reduction reaches 4.46 K,

after which the panel temperature tends to approach a relatively stable state. This behavior can be attributed to the spectral redistribution of the incident solar radiation by the Cu@SiO_2 nanofluid. Specifically, part of the radiation that is less effectively converted into electricity by the c-Si photovoltaic cell is absorbed by the nanofluid and converted into useful thermal energy, thereby reducing the heat load directly imposed on the PV module. It should be emphasized that this intercepted radiation is not useless; rather, it is redirected from direct photovoltaic conversion to photothermal recovery. Therefore, increasing the nanofluid concentration enhances thermal absorption and PV cooling, but it may also reduce the photon flux transmitted to the photovoltaic cell, leading to the decrease in electrical efficiency discussed below. This indicates that the nanofluid concentration should be optimized to balance photovoltaic transmittance loss and thermal energy gain.

Fig. 11b shows the temperature change of the nanofluid in the spectral splitter. At the beginning of the experiment, the temperature rise rate of the nanofluid is faster than after 6 min. This is because as the temperature of the nanofluid increases, the radiative losses become greater, leading to a decrease in initial transient thermal efficiency and a slowdown in temperature rise. The highest temperatures recorded at 10 min are 315.51, 317.01, and 319.05 K, respectively. The higher the mass concentration of the nanofluid, the greater the rate of temperature rise and the maximum temperature. This is because nanofluids with higher mass fractions have stronger photothermal absorption capabilities, enabling them to absorb more sunlight and convert it into thermal energy. The temperature evolution also indicates a clear difference between the initial transient stage and the later heating stage. During the initial stage, the nanofluid temperature was close to the ambient temperature, and the net absorbed solar energy was mainly converted into sensible heat. As the heating process continued, the increased temperature difference between the nanofluid and the surroundings enhanced the heat loss, resulting in a reduced heating rate. Therefore, the thermal efficiency calculated from the first 360 s should be interpreted as an initial transient performance indicator. The 10 min temperature curves were used to confirm the consistency of the concentration-dependent trend.

From a heat-transfer perspective, the absorbed non-PV-band solar radiation is first converted into internal energy of the Cu@SiO_2 nanofluid, leading to a transient temperature rise governed by the effective heat capacity of the base fluid and nanoparticles. During this process, part of the absorbed heat is inevitably dissipated to the surroundings through natural convection from the container surface and long-wave thermal radiation, while the remaining heat is stored as sensible heat in the nanofluid. Increasing the nanoparticle concentration enhances volumetric solar absorption and thermal gain, but it also changes the effective heat capacity and optical transmission of the nanofluid; therefore, the optimal concentration should be determined by balancing photothermal heat collection, heat loss, and photovoltaic transmission.

Fig. 12 shows the system efficiency and merit function (MF) of the SBS-PV/T system. The electrical efficiencies are 15.8%, 9.30%, 7.11%, and 5.75%, while the initial transient thermal efficiencies are 32.36%, 41.4%, and 48.25%, respectively. The overall system efficiencies are 56.84%, 60.12%, and 63.38%. The electrical efficiency is negatively correlated with the mass concentration, while the initial transient thermal efficiency is positively correlated. Nanofluids with higher concentrations have stronger spectral absorption properties, thus typically achieving higher photothermal conversion efficiencies, but also significantly reducing the power generation efficiency of the photovoltaic cells. Therefore, the selection of nanofluid concentration should be balanced based on actual operating conditions. Additionally, the MF values of the nanofluids are all greater than 1, indicating that the losses in photovoltaic cell efficiency due to spectral splitting are completely compensated by the gains in thermal efficiency brought by the spectral splitting system. The highest MF value is 1.3819.

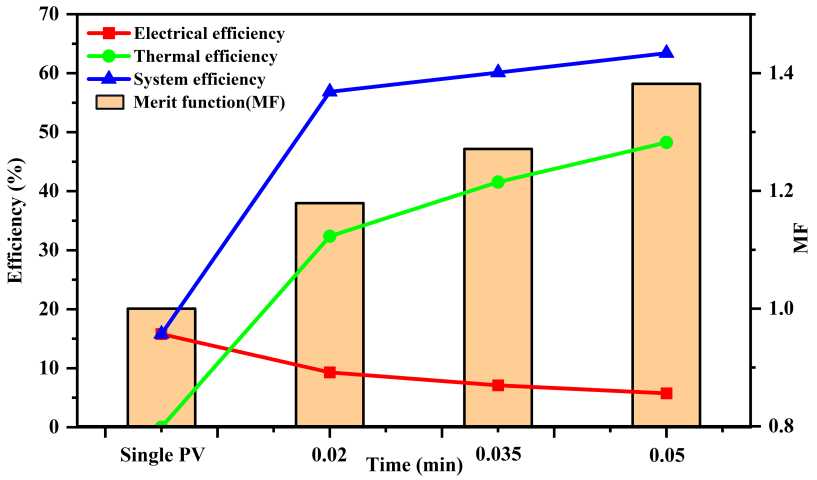

Figure 12: Conversion efficiency and merit function diagram.

It should be noted that the values of 56.84%, 60.12%, and 63.38% represent energy-equivalent efficiencies rather than exergy efficiencies. These values increase with nanofluid concentration because the enhanced spectral absorption improves the first-law thermal energy recovery. However, an exergy-based interpretation would lead to a more conservative evaluation of the recovered heat because the thermal output is low-temperature heat close to the ambient condition. In contrast, the electrical output has much higher energy quality. Therefore, although the 0.05 wt% nanofluid exhibits the highest energy-equivalent efficiency, the exergy-based viewpoint suggests that the electrical-efficiency loss at high concentration should also be carefully considered.

The Table 6 shows that ZnO-based nanofluids can achieve high thermal efficiency, but the reported electrical efficiency and merit function may be relatively limited. ITO-based nanofluids show relatively high electrical efficiency, whereas their reported thermal efficiency is lower. CNT/Ag and Ag-based nanofluids can improve the spectral-splitting performance, but Ag and Au nanoparticles usually involve higher material cost. Compared with these nanofluids, the present Cu@SiO_2 nanofluid shows a competitive balance among electrical output, thermal recovery, and comprehensive system performance. Specifically, the proposed system achieves a maximum electrical efficiency of 9.30%, a maximum thermal efficiency of 48.25%, a maximum overall system efficiency of 63.38%, and a maximum merit function of 1.3819. The merit function is higher than the reported ZnO-based values summarized in the revised comparison, indicating that the thermal gain can effectively compensate for the electrical loss caused by spectral splitting.

Table 6: Benchmarking of the present Cu@SiO_2 nanofluid against representative spectral-splitting nanofluids.

Nanofluid/Splitter	Electrical Efficiency η_e (%)	Thermal Efficiency η_{th} (%)	Overall Efficiency/MF	Benchmarking Implication
ZnO	3.73	76.1	Total: 85.7%; MF: 1.076–1.184	High thermal recovery, but relatively low electrical efficiency and MF compared with the present Cu@SiO_2 case.

(Continued)

Table 6 (continued)

Nanofluid/Splitter	Electrical Efficiency η_e (%)	Thermal Efficiency η_{th} (%)	Overall Efficiency/MF	Benchmarking Implication
ZnO/Cu_9S_5	N.R.	N.R.	Effective spectral transmittance coefficient: ZnO 8.74% higher than Cu_9S_5	Useful optical benchmark; energy-conversion metrics are not fully reported for direct efficiency comparison.
ITO	17.7	18.5	N.R.	Higher electrical efficiency, but lower thermal efficiency than the present Cu@SiO_2 nanofluid.
CNT/Ag	Relative increase: +7.2% vs. Ag; +1.4% vs. CNT	Relative increase: +9.9% vs. Ag; +15.0% vs. CNT	Filtering efficiency: 18.3%	Hybrid plasmonic/carbon absorber improves spectral filtering, but absolute ηe, ηth and MF are not directly available in the same format.
Ag/$CoSO_4$-PG	11.9	49.3	Optical efficiency: 95.5%	Good PV-band matching and thermal recovery; noble-metal Ag increases material cost.
Ag/$CoSO_4$	8.5	56.0	Overall exergy efficiency: 19.6%	Thermal efficiency is slightly higher than Cu@SiO_2, while electrical efficiency is lower; Ag cost remains a limitation.
Ag and Au	N.R.	Au: +6.8%; Ag: +4.8% thermal enhancement	N.R.	Demonstrates plasmonic enhancement, but Au/Ag are expensive compared with Cu.
Present Cu@SiO_2	Max. 9.30	Max. 48.25	System efficiency: 63.38%; MF: 1.3819	Provides a competitive balance of electrical output, thermal recovery, MF, lower material cost, and improved oxidation resistance due to SiO_2 coating.

6 Conclusion

Under the present experimental conditions, water-based Cu@SiO_2 nanofluids showed effective spectral splitting behavior in the SBS-PV/T system. FDTD analysis indicated that 50 nm Cu nanoparticles provide a favorable balance between absorption and scattering in the 300–1000 nm range. Outdoor tests with 0.02, 0.035, and 0.05 wt% nanofluids showed that increasing concentration improved thermal efficiency and energy-equivalent efficiency but reduced electrical efficiency. The maximum energy-equivalent system efficiency was 63.38% at 0.05 wt%, while the highest electrical efficiency was 9.30% at 0.02 wt%. These results demonstrate the potential of Cu@SiO_2 nanofluids for SBS-PV/T applications within the tested concentration range and system configuration. Further work is needed to evaluate long-term stability, scale-up performance, and operation under different climatic and flow conditions.

Acknowledgement: None.

Funding Statement: This research was funded by the Project of Scientific and Technical Supporting Programs of Changzhou (Grant No. CE20235040), Practice Innovation Program of Jiangsu Province (KYCX24_3238).

Author Contributions: The authors confirm contribution to the paper as follows: Conceptualization, Guofen Rui, Jingyu Cao and Haifei Chen; methodology, Guofen Rui, Xiangyu Hu and Jingyu Cao; software, Guofen Rui and Xiangyu Hu; validation, Guofen Rui, Xiangyu Hu, Yibo Zhang and Yangyang Zhu; formal analysis, Guofen Rui and Xiangyu Hu; investigation, Guofen Rui, Xiangyu Hu, Yibo Zhang and Yangyang Zhu; resources, Jingyu Cao and Haifei Chen; data curation, Guofen Rui and Xiangyu Hu; writing—original draft preparation, Guofen Rui; writing—review and editing, Guofen Rui, Jingyu Cao and Haifei Chen; visualization, Guofen Rui; supervision, Jingyu Cao and Haifei Chen; project administration, Jingyu Cao and Haifei Chen; funding acquisition, Haifei Chen. All authors reviewed and approved the final version of the manuscript.

Availability of Data and Materials: Data available on request from the authors. The data that support the findings of this study are available from the corresponding author, Haifei Chen, upon reasonable request.

Ethics Approval: Not applicable.

Conflicts of Interest: The authors declare no conflicts of interest.

References

1. Kandil AA, Awad MM, Sultan GI, Salem MS. Enhancing photovoltaic performance through solar radiation splitting: a beam splitter-assisted hybrid approach with 2-D tracking and PCM integration. J Energy Storage. 2024;75:109692. doi:10.1016/j.est.2023.109692.
2. Song D, Tian W, An B, Wang K. Twofold spectrum split enabling spectral selectivity tailoring and deep temperature decoupling for high exergy efficiency in a concentrating photovoltaic/thermal (PV/T) system. Energy Convers Manag. 2024;303:118153. doi:10.1016/j.enconman.2024.118153.
3. Zhang C, Wang N, Xu H, Ma Z, Qu Z. Development of a fully coupled concentrator-spectral splitter-thermal-electrical model with evaluation of electrical uniformity for full-spectrum photovoltaic/thermal systems. Energy. 2024;313:134106. doi:10.1016/j.energy.2024.134106.
4. Zeng Z, Geng J, Ai C, Ma L, Jing D. Experimental investigation on parameter optimization of liquid spectral beam splitter for continuous photocatalytic hydrogen production accompanied with photovoltaic power generation under solar full spectrum. Int J Hydrog Energy. 2024;56:1202–15. doi:10.1016/j.ijhydene.2023.12.302.
5. Jiao Y, Xing M, Estellé P. Efficient utilization of hybrid photovoltaic/thermal solar systems by nanofluid-based spectral beam splitting: a review. Sol Energy Mater Sol Cells. 2024;265(1):112648. doi:10.1016/j.solmat.2023.112648.
6. Klampaftis E, Congiu M, Robertson N, Richards BS. Luminescent ethylene vinyl acetate encapsulation layers for enhancing the short wavelength spectral response and efficiency of silicon photovoltaic modules. IEEE J Photovolt. 2011;1(1):29–36. doi:10.1109/JPHOTOV.2011.2162720.
7. Hong W, Li B, Li H, Niu X, Li Y, Lan J. Recent progress in thermal energy recovery from the decoupled photovoltaic/thermal system equipped with spectral splitters. Renew Sustain Energy Rev. 2022;167(2):112824. doi:10.1016/j.rser.2022.112824.
8. Chen H, Liu Y, Wang Y, Peng M, Deng S, Yang H. Performance analysis of a low concentrated photovoltaic system thermal management by hybrid phase change materials. Int Commun Heat Mass Transf. 2024;159(2):108025. doi:10.1016/j.icheatmasstransfer.2024.108025.
9. Das D, Kamble AD, Kalita P. Performance investigation of transparent photovoltaic-thermal collector with horizontal oscillating and rectangular spiral flow patterns. Int J Energy Res. 2022;46(1):239–53. doi:10.1002/er.6298.
10. Rubaiee S, Yahya SM, Fazal MA, Danish M. Characterization of Al_2O_3, TiO_2, hybrid Al_2O_3-TiO_2 and graphene oxide nanofluids and their performance evaluations in photovoltaic thermal system. J Therm Anal Calorim. 2023;148(21):11467–77. doi:10.1007/s10973-023-12492-8.
11. Widyolar B, Jiang L, Winston R. Spectral beam splitting in hybrid PV/T parabolic trough systems for power generation. Appl Energy. 2018;209:236–50. doi:10.1016/j.apenergy.2017.10.078.
12. Huang G, Wang K, Markides CN. Efficiency limits of concentrating spectral-splitting hybrid photovoltaic-thermal (PV-T) solar collectors and systems. Light Sci Appl. 2021;10(1):28. doi:10.1038/s41377-021-00465-1.

13. Yu ZJ, Fisher KC, Wheelwright BM, Angel RP, Holman ZC. PVMirror: a new concept for tandem solar cells and hybrid solar converters. IEEE J Photovolt. 2015;5(6):1791–9. doi:10.1109/JPHOTOV.2015.2458571.
14. Mojiri A, Stanley C, Taylor RA, Kalantar-zadeh K, Rosengarten G. A spectrally splitting photovoltaic-thermal hybrid receiver utilising direct absorption and wave interference light filtering. Sol Energy Mater Sol Cells. 2015;139(4):71–80. doi:10.1016/j.solmat.2015.03.011.
15. Liew NJY, Lee HJ. Numerical analysis of hybrid photovoltaic-thermal systems utilizing different spectral bandpass filters. Renew Energy. 2019;144:15–29. doi:10.1016/j.renene.2018.12.016.
16. Meraje WC, Huang CC, Barman J, Huang CY, Kuo CJ. Design and experimental study of a Fresnel lens-based concentrated photovoltaic thermal system integrated with nanofluid spectral splitter. Energy Convers Manag. 2022;258:115455. doi:10.1016/j.enconman.2022.115455.
17. Liang H, Wang F, Li D, Zhu J, Tan J. Optical properties and transmittances of ZnO-containing nanofluids in spectral splitting photovoltaic/thermal systems. Int J Heat Mass Transf. 2019;128(29):668–78. doi:10.1016/j.ijheatmasstransfer.2018.09.032.
18. Abd El-Samie MM, Ju X, Xu C, Du X, Zhu Q. Numerical study of a photovoltaic/thermal hybrid system with nanofluid based spectral beam filters. Energy Convers Manag. 2018;174:686–704. doi:10.1016/j.enconman.2018.08.083.
19. Jiang T, Zou T, Wang G, Wang B, Chen Z. Preparation and application study in a novel solar PV/thermal system of indium tin oxide nanofluid optical filter. Energy Rep. 2022;8:5668–77. doi:10.1016/j.egyr.2022.04.026.
20. Zhang M, Tang L, Duan A, Zhang Y, Xiao F, Zhu Y, et al. Adjusting charge kinetics of conjugated polymers via integration of LSPR effect with homojunction. Chem Eng J. 2023;452:139068. doi:10.1016/j.cej.2022.139068.
21. Hassani S, Saidur R, Mekhilef S, Taylor RA. Environmental and exergy benefit of nanofluid-based hybrid PV/T systems. Energy Convers Manag. 2016;123:431–44. doi:10.1016/j.enconman.2016.06.061.
22. Xia X, Cao X, Li N, Yu B, Liu H. Study on a spectral splitting photovoltaic/thermal system based on CNT/Ag mixed nanofluids. Energy. 2023;271(1):127093. doi:10.1016/j.energy.2023.127093.
23. Wang G, Ge Z, Lin J. Design and performance analysis of a novel solar photovoltaic/thermal system using compact linear Fresnel reflector and nanofluids beam splitting device. Case Stud Therm Eng. 2022;35(5):102167. doi:10.1016/j.csite.2022.102167.
24. Wang G, Chen X, Lin J, Xu C, Ju X. Experimental study on a concentrating solar photovoltaic/thermal system using different fluid spectral beam filters. J Clean Prod. 2023;429:139549. doi:10.1016/j.jclepro.2023.139549.
25. Yang B, Zhi Y, Qi Y, Xie L, Yu X. Advancing performance assessment of a spectral beam splitting hybrid PV/T system with water-based SiO_2 nanofluid. Front Energy. 2024;18(6):799–815. doi:10.1007/s11708-024-0935-7.
26. Zhang G, Shan S, Wu H, Tian J, Cheng Z, Zhou Z. Investigation on the radiative characteristics of ZnO-SiO_2 nanofluids in spectral splitting photovoltaic/thermal systems. Sol Energy Mater Sol Cells. 2024;277(6):113129. doi:10.1016/j.solmat.2024.113129.
27. Wang G, Chou P, Li Y, Xia L, Liu Y, Wei G. Solar spectral beam splitting simulation of aluminum-based nanofluid compatible with photovoltaic cells. Energies. 2025;18(10):2460. doi:10.3390/en18102460.
28. Zhang X, Lei D, Zhang B, Yao P, Wang Z. SiNx/Cu spectral beam splitting films for hybrid photovoltaic and concentrating solar thermal systems. ACS Omega. 2021;6(33):21709–18. doi:10.1021/acsomega.1c03178.
29. Said AB, Tang L, Zhou H, Zhang Y, Li Q. Investigation of Nb_2O_5/SiO_2 short-wave pass filters for beam-splitting application in a PV/CSP solar hybrid system. Appl Opt. 2025;64(5):1196–205. doi:10.1364/ao.550695.
30. Dmour A, Xiao Y, Tian W, Qin G, Zheng X. CQD-ATO hybrid nanofluid with good stability in the application of spectral beam splitters. Sol Energy Mater Sol Cells. 2023;261(1):112536. doi:10.1016/j.solmat.2023.112536.
31. Li Z, Jia L, Li Y, He T, Li XM. Ammonia-free preparation of Ag@SiO_2 core/shell nanoparticles. Appl Surf Sci. 2015;345:122–6. doi:10.1016/j.apsusc.2015.03.159.
32. An W, Chen L, Liu T, Qin Y. Enhanced solar distillation by nanofluid-based spectral splitting PV/T technique: preliminary experiment. Sol Energy. 2018;176(1):146–56. doi:10.1016/j.solener.2018.10.029.
33. Qi Y, Liu Z, Shi Y, Yu X, Yang B. Size optimization of nanoparticle and stability analysis of nanofluids for spectral beam splitting hybrid PV/T system. Mater Res Bull. 2023;162:112184. doi:10.1016/j.materresbull.2023.112184.

34. Chen M, He Y, Wang X, Hu Y. Numerically investigating the optical properties of plasmonic metallic nanoparticles for effective solar absorption and heating. Sol Energy. 2018;161:17–24. doi:10.1016/j.solener.2017.12.032.
35. Han X, Guo Y, Wang Q, Phelan P. Optical characterization and durability of immersion cooling liquids for high concentration III–V photovoltaic systems. Sol Energy Mater Sol Cells. 2018;174:124–31. doi:10.1016/j.solmat.2017.08.034.
36. Wang S, Feng K, Zhang D, Yang D, Xiao M, Zhang C, et al. Stable Cu catalysts supported by two-dimensional SiO_2 with strong metal-support interaction. Adv Sci. 2022;9(9):2104972. doi:10.1002/advs.202104972.
37. Jiang F, Lan T, Sun J, Zhao G, Lu Y. Core-shell $Cu@SiO_2/SiO_2$ catalyst for 1, 6-hexanediol dehydrogenation to ε-caprolactone: high activity and stability from core-shell nanostructure. Nano Res. 2023;16(10):12270–80. doi:10.1007/s12274-023-5891-8.
38. Ismail MF, Azmi WH, Mamat R, Sharma KV, Ali HM. Extensive stability assessment of TiO_2/polyvinyl ether nanolubricant with physical homogenization. Lubricants. 2023;11(2):67. doi:10.3390/lubricants11020067.
39. Mukherjee S, Chakrabarty S, Mishra PC, Chaudhuri P. Stability and sedimentation characteristics of water based Al_2O_3 and TiO_2 nanofluids. Proc Inst Mech Eng Part N J Nanomater Nanoeng Nanosyst. 2024;238(1–2):17–30. doi:10.1177/23977914221127735.
40. Fang H, Ma J, Du T, Chen Q, Chen H, Tong W, et al. Performance evaluation of an improved unglazed photovoltaic and thermal hybrid system. J Energy Resour Technol. 2022;144(10):101303. doi:10.1115/1.4053951.
41. Huang J, Han X, Zhao X, Meng C. Facile preparation of core-shell $Ag@SiO_2$ nanoparticles and their application in spectrally splitting PV/T systems. Energy. 2021;215(2):119111. doi:10.1016/j.energy.2020.119111.
42. Chen H, Chen X, Hong T, Du P, Peng M, Deng S, et al. Investigation on the performance of a solar multifunctional photovoltaic/thermal window combining photocatalytic oxidation technology. Renew Energy. 2024;235(21):121371. doi:10.1016/j.renene.2024.121371.
43. Han X, Xue D, Zheng J, Alelyani SM, Chen X. Spectral characterization of spectrally selective liquid absorption filters and exploring their effects on concentrator solar cells. Renew Energy. 2019;131(10):938–45. doi:10.1016/j.renene.2018.07.125.
44. Chen L, Deng D, Ma Q, Yao Y, Xu X. Performance evaluation of high concentration photovoltaic cells cooled by microchannels heat sink with serpentine reentrant microchannels. Appl Energy. 2022;309(4):118478. doi:10.1016/j.apenergy.2021.118478.
45. Tang Z, Liu X, Liu X, Wu J, Lin W, Lin X, et al. Unclonable anti-counterfeiting labels based on plasmonic-patterned nanostructures. Adv Eng Mater. 2022;24(9):2101701. doi:10.1002/adem.202101701.
46. Lamba TK, Augustine S, Saini M, Sooraj KP, Ranjan M. LSPR anisotropy minimization by sequential growth of Ag nanoparticles on nanoripple patterned Si surface for SERS Application. Surf Interfaces. 2024;52:104852. doi:10.1016/j.surfin.2024.104852.